Probing the position-dependent optical energy fluence rate in three-dimensional scattering samples

Ozan Akdemir,* Minh Duy Truong, Alfredo Rates, Ad Lagendijk, and Willem L. Vos†
Complex Photonic Systems (COPS), MESA + Institute for Nanotechnology, University of Twente, P.O. Box 217, 7500 AE Enschede, The Netherlands

(Received 26 January 2024; accepted 29 July 2024; published 18 September 2024)

The accurate determination of the position-dependent energy fluence rate of scattered light (which is proportional to the energy density) is crucial to the understanding of transport in anisotropically scattering and absorbing samples, such as biological tissue, seawater, atmospheric turbulent layers, and light-emitting diodes. While Monte Carlo simulations are precise, their long computation time is not desirable. Common analytical approximations to the radiative transfer equation (RTE) fail to predict light transport and could even give unphysical results. Therefore, we experimentally probe the position-dependent energy fluence rate of light inside scattering samples where the widely used P_1 and P_3 approximations to the RTE fail. The samples are three-dimensional (3D) aqueous suspensions of anisotropically scattering and both absorbing and nonabsorbing spherical scatterers, namely, microspheres ($r = 0.5$ μm) with and without absorbing dye. To probe the energy fluence rate, we detect the emission of quantum-dot reporter particles that are excited by the incident light and that are contained in a thin capillary. By scanning the capillary through the sample, we access the position dependence. We present a comprehensive discussion of experimental limitations and of both random and systematic errors. Our observations agree well with the Monte Carlo simulations and the P_3 approximation of the RTE with a correction for forward scattering. In contrast, the P_1 and the P_3 approximations deviate increasingly from our observations, ultimately even predicting unphysical negative energies.

DOI: 10.1103/PhysRevA.110.033520

I. INTRODUCTION

For myriad applications such as light emitting diodes (LEDs) [1–8], atmospheric aerosols [9], oceanography and remote sensing [10–16], and biophysics [17–20], as well as for fundamental physics like phase-conjugated scattering [21], random lasing [22], correlated and inhomogeneous scattering media [23–25], and metamaterials [26], it is crucial to understand the light transport. Hence, it is vital to predict the position-dependent energy fluence rate that is proportional to the energy density. While Monte Carlo simulations are a powerful tool to study the energy distribution in scattering media [27–35], they come at the cost of extremely long computation times [36]. Analytical approximations to transport theory offer a much faster alternative [37–44], but they may not provide accurate results for samples that exhibit strong anisotropic scattering and absorption [45].

Experimental observations of the position-dependent energy fluence rate in real scattering samples are essential to identify reliable methods to model the light transport in real devices. Such *in situ* and *in vitro* measurements of light transport have been widely made in different research areas, including aerosols [46,47], LEDs [48], and photodynamic therapy [49–51].

In Ref. [45] we studied several analytic models of light transport that are summarized in Appendix B and presented their ranges of validity as well as their accuracies, as gauged by Monte Carlo simulations. As a next step, we decided to observe what happens in real samples where analytic models break down. As an illustrative example, Fig. 1 shows the measured and modeled energy fluence rate $\Phi(z)$ of a forward-scattering and moderately absorbing sample that lies in the unphysical range of the P_3 approximation to the radiative transfer equation. Naively, one would solely trust Monte Carlo simulations, but it is important to note that even the best simulation cannot fully replicate experimental observations. For instance, Monte Carlo simulations of light transport rely on input parameters such as scattering and absorption coefficients, which are typically interpreted from other experiments that carry additional assumptions and errors. Hence, accurate experimental observations are ultimately indispensable for device applications in, for instance, semiconductor metrology, solid-state lighting, and space observation optics, all of which are actual applications of our research program [52].

In this work, we report on experiments done in parameter ranges where most of the analytic approximations fail, to observe what happens and how well models pertain. The energy fluence rate $\Phi(\mathbf{r}, \nu)$ represents the total optical power through a unit spherical area, with units $\mathrm{Wm}^{-2}\,\mathrm{Hz}^{-1}$. We simplify the representation of the three-dimensional position $\mathbf{r}$ to a one-dimensional z dependence by considering the total rate versus z position in a cross section (see Fig. 2). For notational ease, we omit the frequency ν dependence to write the position-dependent energy fluence rate as $\Phi(z)$, since our

*Contact author: o.akdemir@utwente.nl
†Contact author: w.l.vos@utwente.nl

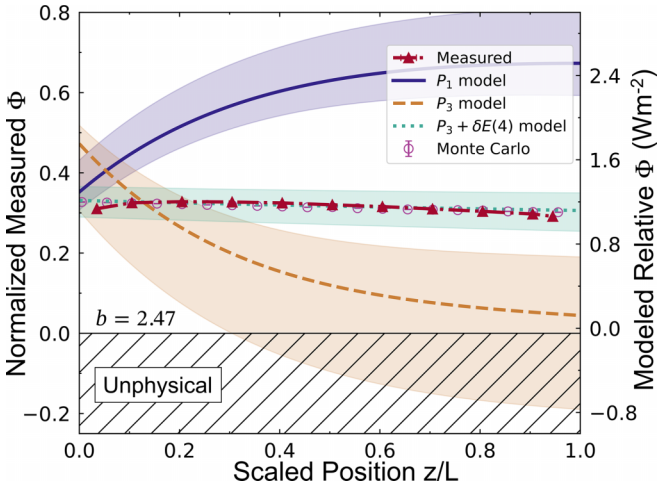

FIG. 1. Measured (red triangles) and modeled energy fluence rate $\Phi(z)$ as a function of depth z, for a sample with optical thickness $b = \mu_{\text{ext}}(\lambda)L = 2.47$. The measured $\Phi(z)$ is normalized to the incident intensity. The curves represent the P_N approximations to the radiative transfer equation and the circles are Monte Carlo simulations. The unphysical range with negative Φ is highlighted with black hatched lines.

study is a nearly monochromatic one. We present our experiments on the *in situ* detection of the position-dependent fluence rate $\Phi(z)$ in both absorbing and nonabsorbing, anisotropically scattering samples. We compare the experiments to well-known theoretical models, namely, the P_1, P_3, and $P_3 + \delta E(4)$ approximations to the radiative transfer equation, and to Monte Carlo simulations of light transport, where the method of simulations used here is adapted from Ref. [29].

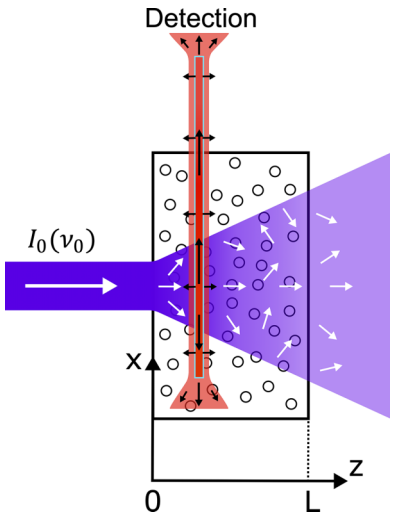

FIG. 2. Cross section of a slab with thickness L that contains an aqueous suspension of microspheres. A thin capillary filled with fluorescent reporters is inserted in the sample as a probe. The slab is illuminated from the side by light with intensity $I_0(\nu_0)$. The white arrows represent the direction of light with frequency ν_0, including both the diffuse and the unscattered parts. The black arrows represent the direction of emitted light with frequency ν_e. Fluorescent emission is detected from the top of the probe.

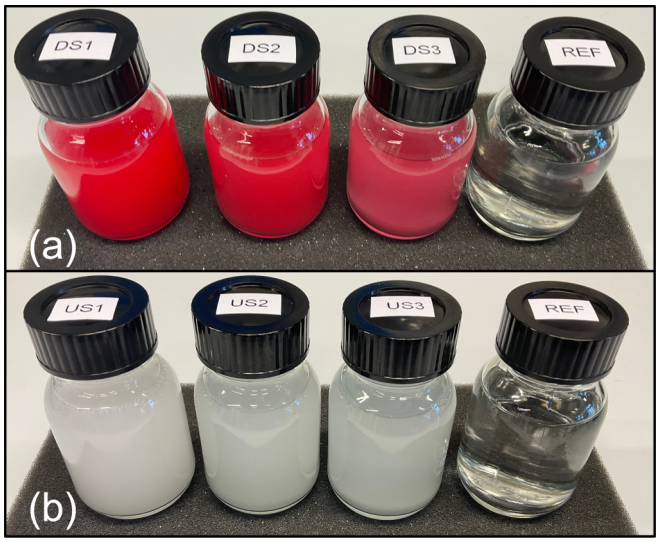

FIG. 3. Photographs of the suspensions with different densities of (a) red dyed scatterers and (b) undyed scatterers. The scatterers are polystyrene spheres with $D = (1.00 \pm 0.05)$ μm diameter.

A schematic of our experimental method is shown in Fig. 2, where a slab with spherical scatterers is illuminated from the (x, y) side by light with intensity $I_0(\nu_0)$. Light enters the sample and propagates inside, undergoing scattering and absorption by the spheres. A probe consisting of a thin cylindrical capillary, filled with quantum-dot reporter particles, is utilized to detect the intensity at known positions inside the sample (see, e.g., Refs. [53–55]). When the light reaches the probe from any direction, it excites the quantum-dot reporters that subsequently emit light at a Stokes-shifted lower frequency ν_e. Part of the reemitted light is then collected from the top of the probe, and the position-dependent energy fluence rate is inferred from this measurement. Our observations match well with physical and accurate models for these types of samples and show a clear distinction from the ones that fail and predict *unphysical* negative-energy fluence rates.

II. EXPERIMENTAL DETAILS

The experiments are done on samples with strongly forward-scattering (anisotropy $g > 0.75$) and absorbing (albedo $a < 1$) scatterers, to be in the parameter range where common analytical approximations fail [45].

A. Sample preparation

Samples are prepared by diluting commercially bought polystyrene microsphere suspensions, with reported particle radii $r = 0.5 \pm 0.025$ μm. The microsphere suspensions used in our experiments are both plain and red-dyed Polybead® polystyrene microspheres from Polysciences for undyed and dyed sphere suspensions, respectively. A buffer solution is produced by mixing sodium dodecyl sulfate (SDS) surfactant (0.05%) with de-ionized (DI) water (99.95%). The samples with scatterers are then prepared by diluting their respective suspensions with the buffer solution, where syringe filters with 0.2-μm pore size are used to remove residual particles

TABLE I. Contents and number density of scatterers ρ of the prepared samples. The percentages of spheres are adjusted from the information provided by the vendor about their products. The DS are red-dyed microsphere samples and US are undyed microsphere samples.

Sample name	Contents	ρ (mm^{-3})
Reference	99.95 wt. % DI water + 0.05 wt. % SDS	0
DS1	0.025% (wt./vol) dyed sphere + Ref	$(4.6 \pm 0.6) \times 10^5$
DS2	0.013% (wt./vol) dyed sphere + Ref	$(2.3 \pm 0.3) \times 10^5$
DS3	0.006% (wt./vol) dyed sphere + Ref	$(1.1 \pm 0.1) \times 10^5$
US1	0.026% (wt./vol) plain sphere + Ref	$(4.7 \pm 0.6) \times 10^5$
US2	0.013% (wt./vol) plain sphere + Ref	$(2.4 \pm 0.3) \times 10^5$
US3	0.007% (wt./vol) plain sphere + Ref	$(1.2 \pm 0.2) \times 10^5$

from the buffer solution. The use of SDS in the buffer solution serves to stabilize the colloidal suspension and prevent agglomeration and sedimentation of the scatterers. The samples prepared with this buffer solution are stable for at least 24 h, after which some initial sedimentation is observed. Prior to experiments, the samples are carefully agitated, with attention paid to prevent the introduction of air bubbles. Overall, based on our previous detailed colloidal studies [56–59], we estimate the fraction of nonsingle spheres to be less than about 5%; hence Mie theory for single spheres is valid for our samples. Dyed sphere samples are labeled DS, and plain (undyed) sphere samples are US. A photograph of the samples is shown in Fig. 3, showing the different diffuse color appearance of the DS samples and different whiteness of the US samples. The contents and scatterer concentrations of prepared samples are listed in Table I. Since the weight fraction of polystyrene spheres in water is closely equal to the volume fraction and since all our suspensions have a volume fraction less than 0.026 vol %, the structure factors of our suspensions are very nearly equal to $S(Q) = 1$ [60]; hence Monte Carlo simulations of light transport do not require structural corrections [61].

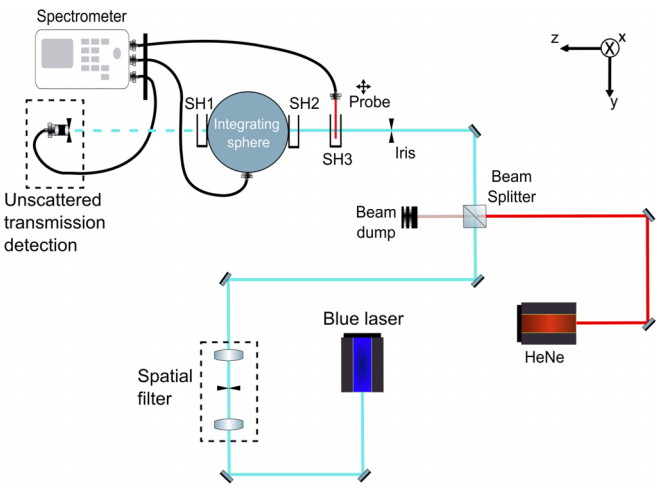

FIG. 4. Schematic of the experimental setup. The blue laser ($\lambda = 408.5$ nm) is the primary light source that is spatially filtered and combined with the HeNe laser at the beam splitter for alignment purposes. The probe is attached to an assembly of motorized translation stages for precise positioning in three dimensions. The spectrometer is connected to the probe, integrating sphere, and unscattered transmission detection via fiber-optic cables. Several components, including ND filters and beam dumps, have been omitted for clarity.

B. Experimental setup

Figure 4 presents a schematic of the setup used in our experiments. A blue laser (Thorlabs NPL41B, $\lambda = 408.5$ nm) is used as the primary light source (see Appendix A 1). The laser beam is spatially filtered because multiple modes inside the laser cavity are not collimated as well as the fundamental mode, while they perturb the beam profile at the sample. A substantial improvement is observed upon spatial filtering (see Ref. [62]).

The sample holders SH1 and SH2 are attached to the integrating sphere, whereas the holder SH3, where the probe is immersed (see Figs. 4 and 5), is positioned separately from the integrating sphere. The probe is connected to a custom-built holder with three-dimensionally printed and manually made parts, as shown in Fig. 5. For details on the preparation of the probe, see Appendix A 2. To detect the intensity emitted from the probe, a connector part is created in the workshop to connect the probe with a fiber-optic cable that is attached to a spectrometer (Avantes Starline, AvaSpec-2048L) on the other end. The holder is attached to an assembly of motorized translation stages (Thorlabs MTS50/M-Z8) that moves the probe to precise positions in three dimensions. In-house PYTHON scripts are used to control the movement of the probe and detection with the spectrometer. The x-direction movement is

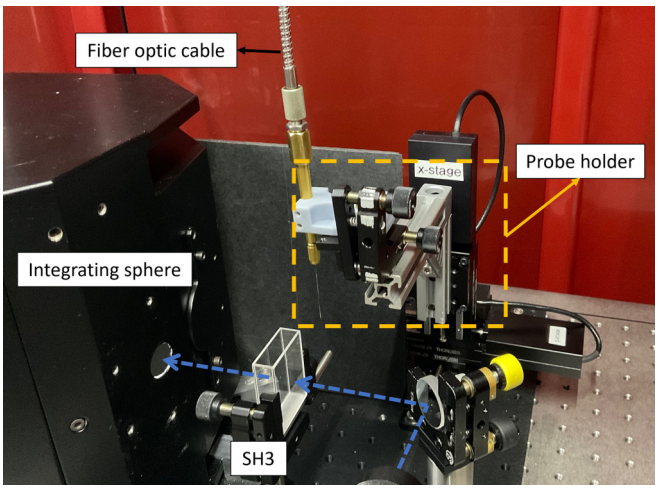

FIG. 5. Photograph of the assembled probe holder. The fiber attached to the probe, the integrating sphere transmission port, and the sample holder SH3 with an empty cuvette attached to it are also visible in the photo.

utilized to move the probe in and take it out of the sample, whereas the y- and z-direction movements are used to scan the sample and measure the intensity at specific positions. Total transmission and total reflection measurements are done with an integrating sphere (Opsira UKU240), with a port diameter $d_{\text{port}} = 20$ mm for both transmission and reflection ports.

Before collecting data, each sample suspension is transferred to a wide quartz cuvette (outer dimensions $12.5 \times 32.5 \times 45$ mm) with an inner thickness of $L = 10$ mm along the z direction, as is shown in Fig. 5. These cuvettes are then placed in sample holders for measurements. The holders SH1 and SH2 are used for total reflection and total transmission measurements, respectively. Holder SH3, shown in Fig. 5, is used in the measurements with the probe and to measure unscattered transmission T_{u} that represents the light that survives extinction while maintaining its original direction. The distance between the fiber coupler of T_{u} detection and SH3 is 750 mm, which results in a half-acceptance angle $\theta = 0.04^{\circ}$. The fraction of detected scattered light is estimated to be less than 0.1% in our T_{u} measurements [63].

III. RESULTS AND DISCUSSION

In this section, the results of unscattered transmission, total transmission, total reflection, and probe measurements are discussed. In addition, the method to extract the albedo a and the anisotropy g of the samples is discussed.

A. Unscattered transmission, total transmission and total reflection

The unscattered transmission T_{u} represents the portion of the incident light that is transmitted through the sample without deviating from its initial direction of travel. Usually, the Beer-Lambert-Bouguer law is used to express T_{u} as

$$T_{\text{u}}(\lambda, \rho) = \frac{I_{\text{u}}(\lambda, \rho)}{I_0(\lambda)} = e^{-\rho\sigma_{\text{ext}}(\lambda,\rho)L}. \tag{1}$$

Here I_{u} is the intensity transmitted without changing its direction, I_0 is the incident intensity, ρ is the number density, σ_{ext} is the extinction cross section, and L is the sample thickness. Furthermore, the optical thickness b is defined to be

$$b(\lambda, \rho) \equiv \rho\sigma_{\text{ext}}(\lambda)L = \mu_{\text{ext}}(\lambda)L, \tag{2}$$

where μ_{ext} is the extinction coefficient. Figure 6(a) presents the measured unscattered transmission T_{u} and Fig. 6(b) displays the extracted optical thickness [see Eq. (2)] of samples DS2, DS3, US2, and US3 throughout the bandwidth of the blue laser. The densest samples DS1 and US1 have a vanishing transmission below our detection limit and are not shown. Therefore, the optical thicknesses of DS1 and US1 are calculated from the measurements of other samples, by appropriately scaling the density of scatterers. The results show a clear effect of the density of scatterers and the composition of the scatterers on the light transmission. Naively, one would expect dyed samples to be optically thicker than undyed samples with similar scatterer concentrations due to increased absorption, but our measurements show the opposite behavior. We attribute this intriguing result to the presence of the unknown red dye inside the scatterers that alters the refractive index of the polystyrene spheres in DS2 and DS3. The dye likely increases the anisotropy, causing the spheres to scatter light more in the forward direction.[1] Consequently, the unscattered part of the transmitted light increases, which explains our observations in Fig. 6.

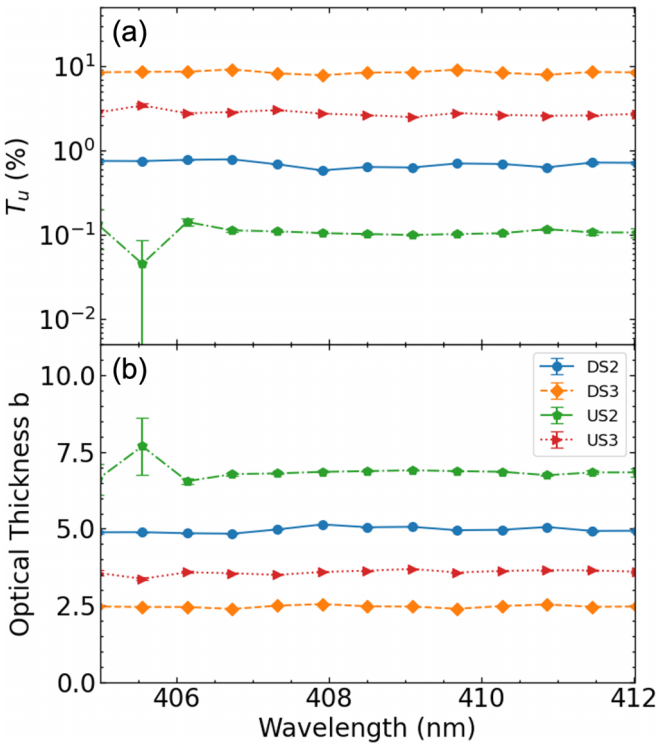

FIG. 6. (a) Unscattered transmission T_{u} and (b) extracted optical thickness b of samples DS2, DS3, US2, and US3.

Total transmission (TT) and total reflection (TR) of dyed and undyed microsphere suspensions are displayed in Fig. 7 as a function of their optical thicknesses at the central wavelength $\lambda = 408.5$ nm. As the optical thickness b increases, both TT and TR decrease for the dyed microspheres [see Fig. 7(a)]. The decrease in TT matches with increased absorption and increased scattering. The simultaneous decrease in TR agrees with the increasing density of forward-scattering microspheres and the increasing absorption when the suspensions get optically thicker.

Since the scatterers in the dyed microsphere suspensions are filled with an unknown red dye (the manufacturer was unable to share the information with us), we cannot use Mie theory to obtain the albedo and anisotropy (a, g), since

[1]We performed Mie scattering calculations for relevant parameters, namely, a sphere with diameter $D = 1.0$ μm and the real part of the refractive index $n_{\text{s}}' = 1.61$, in a medium with $n_{\text{out}} = 1.33$ typical of water at wavelength $\lambda = 0.4085$ μm, and for increasing imaginary sphere index $n_{\text{s}}'' = 0.0004$ (undyed), 0.01, 0.1, and 0.2, resulting in $g = 0.919$, 0.924, 0.950, and 0.954, respectively, thus agreeing with our hypothesis. If we further increase the imaginary part to $n_{\text{s}}'' = 1$ (unrealistic), the anisotropy decreases to $g = 0.871$. For reference, in the case of gain ($n_{\text{s}}'' < 0$) [64], we find that g decreases increasingly rapidly, to a point where $g < 0$, the albedo becomes absurdly large, and a divergence in Mie resonance linewidth occurs [65].

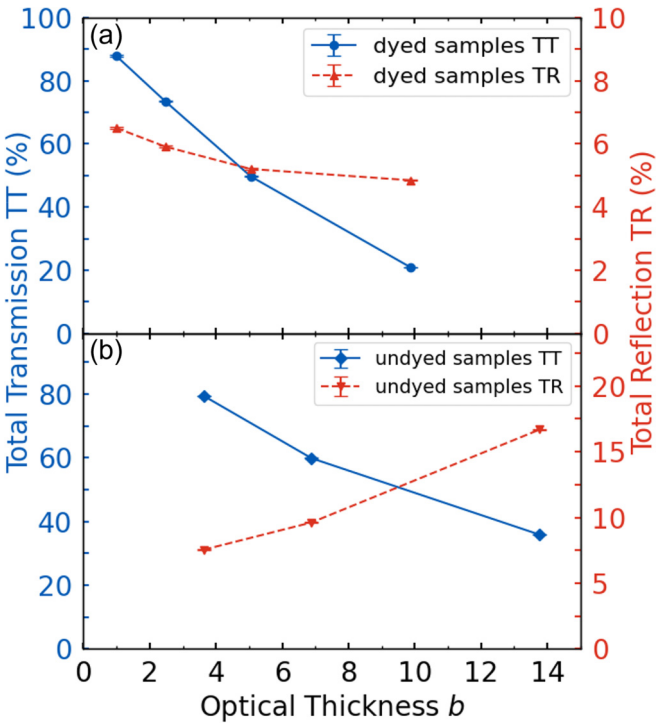

FIG. 7. Total transmission TT(b) and total reflection TR(b) as a function of optical thickness for (a) dyed microsphere suspensions and (b) and undyed microsphere suspensions. The lines connect the data points.

the complex refractive index of the scatterers is unknown. Therefore, our TT and TR measurements are necessary to determine the (a, g) scattering parameters of the dyed samples using models such as P_N approximations to the radiative transfer equation and Monte Carlo simulations of light transport. While the random errors in the measurements are negligibly small (see Fig. 7), systematic errors merit attention during the determination of the scattering parameters.

For the samples with dyed scatterers, systematic errors are more significant at low scatterer density, where the absorption is low. The reason is that the suspensions are held in quartz cuvettes and escaping light reflects multiple times from the cuvette walls before leaving the sample. Hence, light exits the sample and cuvette at wider angles, corresponding to a increased diffuse spot whose size exceeds the port sizes of the integrating sphere. This effect is notable in total reflection, since here light is incident on the sample at 6° off the normal due to the (generic) design of the integrating sphere. If the sample absorption is strong, this effect becomes minor since the internally reflected light is quickly attenuated; hence the angular spread is not substantial. Since errors are largest at lowest densities and since we know that the zero-density reference sample (buffer solution with SDS) has $a = 1$ and $g = 1$, we estimate maximum systematic errors in both TT and TR by comparing the measurements to the Monte Carlo simulations for this reference sample. This comparison yields maximum systematic errors $\Delta TT = 6\%$ in total transmission and $\Delta TR = 4\%$ in total reflection. We utilize these errors to extract a range of possible (a, g) parameters for each dyed sample and we take the average of that range as the extracted (a, g) pair. While the determination of the (a, g) parameters is best for the densest dyed samples, we will see below that the parameters obtained from all samples are in good mutual agreement.

For undyed sphere suspensions, Fig. 7(a) shows that TT decreases with increasing scatterer density (or increasing optical thickness), as expected (see, e.g., [66–68]). In contrast to the dyed microspheres, Fig. 7(b) shows that TR increases with increasing optical thickness, since the light that is less transmitted [compare Fig. 7(a)] is necessarily diffusely reflected, and since absorption is negligible, no light gets lost in the bulk of the samples.

From the reasoning above about reflected light escaping undetected in weakly absorbing samples, we conclude that the systematic error in TR is greater for undyed sphere samples than for the dyed spheres, since the amount of light escaping at even greater angles has increased further. As an illustration, the theoretically computed total reflection for sample US2 is $TR_{P_3+\delta E(4)} = 28.4\%$, whereas the measured total reflection is much less, namely, $TR_{expt} = 10\%$. In contrast, the systematic error in total transmission is much less, as illustrated by theoretical total transmission for US2 being $TT_{P_3+\delta E(4)} = 65.6\%$, which is in good agreement with the measured total transmission $TR_{expt} = 61\%$. Therefore, even though TT agrees well, our extraction method is not able to obtain (a, g) parameters for undyed spheres, since TR is substantially off. Therefore, we employ Mie theory for undyed spheres.

B. Determining (a, g) parameters of the samples

In this section, the albedo and anisotropy (a, g) of dyed microsphere suspensions are obtained by comparing TT and TR measurements to Monte Carlo simulations of light transport, using a brute-force approach. We emphasize that internal reflections from cuvette walls are included in the Monte Carlo simulations to obtain results as close as possible to our measurements. First, the optical thicknesses b of the samples are extracted and then Monte Carlo simulations of light transport are performed for a grid of (a, g) pairs covering all possible albedos and anisotropies. We then use the relative cost function $S(a, g)$ defined as

$$S(a, g) \equiv \sqrt{\delta TT(a, g, a_0, g_0) + \delta TR(a, g, a_0, g_0)}, \quad (3)$$

where the squared relative distances $\delta TR(a, g, a_0, g_0)$ and $\delta TR(a, g, a_0, g_0)$ are equal to

$$\delta TT(a, g, a_0, g_0) = \frac{[TT_{MC}(a, g) - TT_{DS\#}(a_0, g_0)]^2}{TT^2_{DS\#}(a_0, g_0)},$$
$$\delta TR(a, g, a_0, g_0) = \frac{[TR_{MC}(a, g) - TR_{DS\#}(a_0, g_0)]^2}{TR^2_{DS\#}(a_0, g_0)}, \quad (4)$$

$TT_{MC}(a, g)$ and $TR_{MC}(a, g)$ are the total transmission and reflection from Monte Carlo simulations, respectively, $TT_{DS\#}(a_0, g_0)$ and $TR_{DS\#}(a_0, g_0)$ are measured, (a, g) is the running coordinate in the albedo-anisotropy grid, and (a_0, g_0) is the albedo-anisotropy pair of the sample that we want to extract. For the measured $TT_{DS\#}(a_0, g_0)$ and $TR_{DS\#}(a_0, g_0)$ quantities, # represents the number of the sample name, given in Table I.

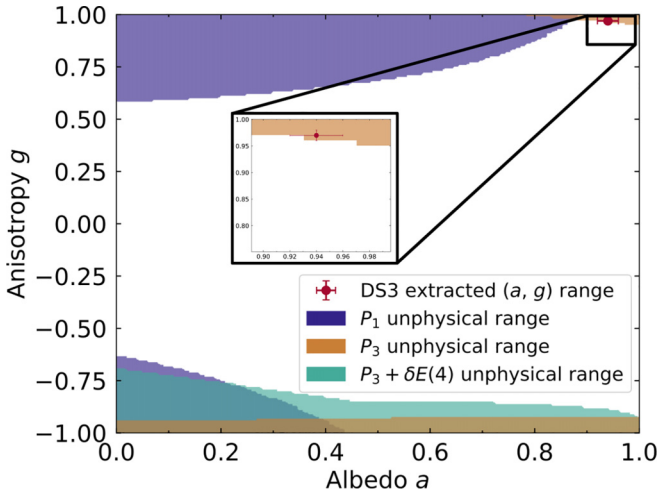

FIG. 8. Extracted parameter range (a, g) using the cost function $S(a, g)$ for sample DS3 with optical thickness $b = 2.47$, shown with the unphysical ranges of the P_1, P_3, and $P_3 + \delta E(4)$ approximations. The inset highlights the extracted (a, g) typical of a forward scattering and absorbing sample.

Figure 8 shows the extracted parameters for sample DS3 ($b = 2.47$) using the brute-force method explained above. In addition, Fig. 8 shows the unphysical ranges of P_1, P_3, and $P_3 + \delta E(4)$ approximations for the sample with optical thickness $b = 2.47$. The horizontal and vertical axes represent all possible albedo a and anisotropy g values, respectively. The minimum cost $S(a, g)$ (the best fit) is found, as expected, in the strong-forward-scattering and moderately absorbing region of the (a, g) grid, which is in the unphysical range of P_3 approximation.[2] However, it is noteworthy that the best fit to our measurements is at $g_0 = 1$, which is an extreme point and is realistically unattainable in real samples with scatterers.[3] This implies that errors in our measurements have a significant effect on the determination of the (a, g) parameters of the samples. We utilize the errors ΔTT and ΔTR reported in Sec. III A to extract the (a, g) parameters of the dyed samples. The extracted (a, g) parameters of the dyed microsphere suspension samples are given in Table II, which shows that the dyed samples are strongly forward scattering and have a moderate absorption. We note that the mutual agreement between the (a, g) parameters obtained for the different samples is very good, within $\delta(a) < 2\%$ for the albedo and $\delta(g) < 1\%$ for the anisotropy, which is even better than expected from the systematic errors discussed above. The comparison between simulated and measured transmission and reflection signals is not necessary for the undyed microsphere suspensions, as their optical properties are obtained directly from Mie theory for spheres. From previous characterization studies [56,69], it is known that such microspheres are highly spherical; hence Mie theory that pertains to spheres gives an excellent description of the scattering properties. The complex refractive index of polystyrene spheres at 408.5 nm is taken from Ref. [70] to be $n_{\text{poly}} = 1.61 + 0.0004i$, which yields nonabsorbing $a = 0.997$ and strong forward scattering $g = 0.919$ for the undyed microspheres suspended in DI water. Mie calculations also provide the extinction cross section σ_{ext}, which we utilize together with the uncertainty of the scatterer radius $\Delta r_{\text{scat}} = \pm 0.03$ μm to determine the 13% uncertainty in the reported densities listed in Table I. The extracted (a, g) parameters for both dyed and undyed samples lie within the range where both P_1 and P_3 approximations fail, whereas the $P_3 + \delta$E(4) approximation is expected to give accurate results.

[2]Remarkably, physical ranges do not imply better accuracy [45].

[3]As the extreme points are not physical, they are not considered in $S(a, g)$ calculations.

TABLE II. Extracted albedo a and anisotropy g values of dyed microsphere suspension samples DS1, DS2, and DS3. The values reported here are averaged over the extracted range of (a, g) pairs and errors are the standard deviation of the mean.

Sample name	Extracted a	Extracted g
DS1	0.90 ± 0.02	0.95 ± 0.02
DS2	0.91 ± 0.01	0.96 ± 0.02
DS3	0.94 ± 0.02	0.97 ± 0.01

C. Position-dependent energy fluence rate of dyed microsphere suspensions

To determine the position-dependent energy fluence rate $\Phi(z)$, the light intensity at specific points inside samples is measured using the experimental setup described in Sec. II B. The coordinate system adopted in this section is depicted in Fig. 4. The objective is to infer $\Phi(z)$ from measurements of the emission of quantum dots inside the probe, which are excited by the blue light inside the sample, along z from the left boundary at $z = 0$ where the incident light enters to the right boundary at $z = 10$ mm. For the details of the probing procedure, see Appendix A 3. The experimental data are compared to Monte Carlo simulations and analytical P_1, P_3, and $P_3 + \delta E(4)$ approximations to the radiative transfer equation [45]. Figure 9 presents the comparison between the models and our measurements. The P_1 and P_3 approximations are not shown as they demonstrate poor accuracy (see Fig. 10). The green areas in Fig. 9 represent the modeled values for the extracted (a, g) range using the $P_3 + \delta E(4)$ approximation. The horizontal axis represents the z positions scaled by the thickness of the sample, whereas the left ordinate displays the $\Phi(z)$ measurements of samples normalized to the measured the incident intensity, which is presented in Fig. 12(b). The ordinate corresponds to the modeled relative $\Phi(z)$. Both ordinates are scaled to compare the trends of measured and modeled Φ, and a good mutual agreement is observed. We define a straightforward proportionality, neglecting the small random errors in measurements,

$$\Phi_{\text{real}}(z) \equiv K \Phi_{\text{measured}}(z), \tag{5}$$

where K is a constant that represents the portion of Φ that is measured. Here K mainly depends on the experimental limitations that are discussed below in Sec. III E. The small differences in measured and modeled Φ trends, excluding the scaling discussed above, are attributed to the limitations of the Henyey-Greenstein phase function [71].

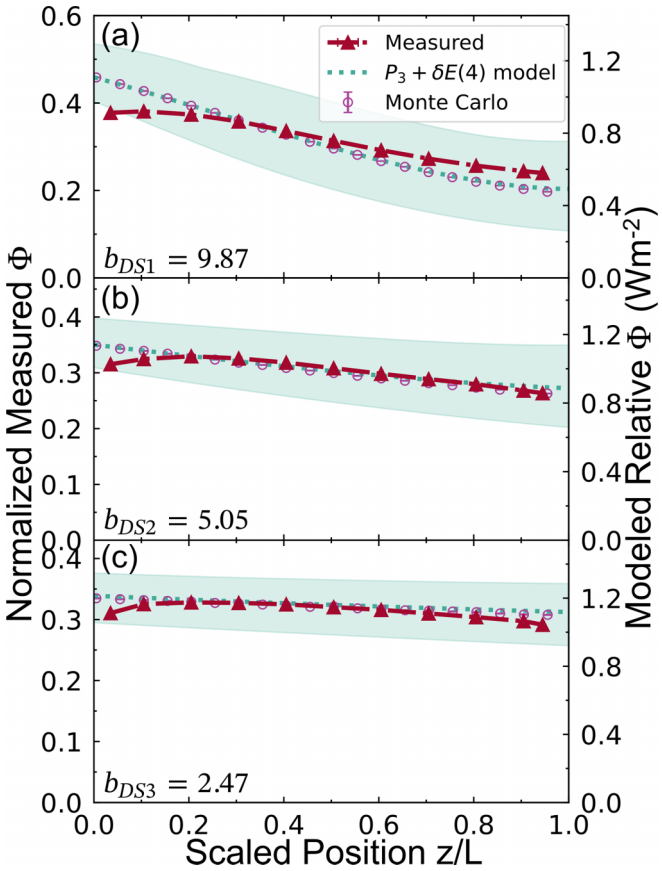

FIG. 9. Comparison of measurement and models for samples (a) DS1, (b) DS2, and (c) DS3. The horizontal axis represents the z positions scaled by the thickness of the sample. The vertical axis on the left displays the $\Phi(z)$ measurements of samples normalized to the measurements of the incident intensity. The right vertical axis corresponds to the modeled relative $\Phi(z)$. The dotted lines represent the calculated $\Phi(z)$ from the $P_3 + \delta E(4)$ approximation. The dynamic range of the $P_3 + \delta E(4)$ approximation is shown as the green area. The circles represent the results of Monte Carlo simulations and the triangles connected by red dash-dotted lines represent the measured results of samples. The measured results are calculated by integrating the y scans at each z position, shown as triangles.

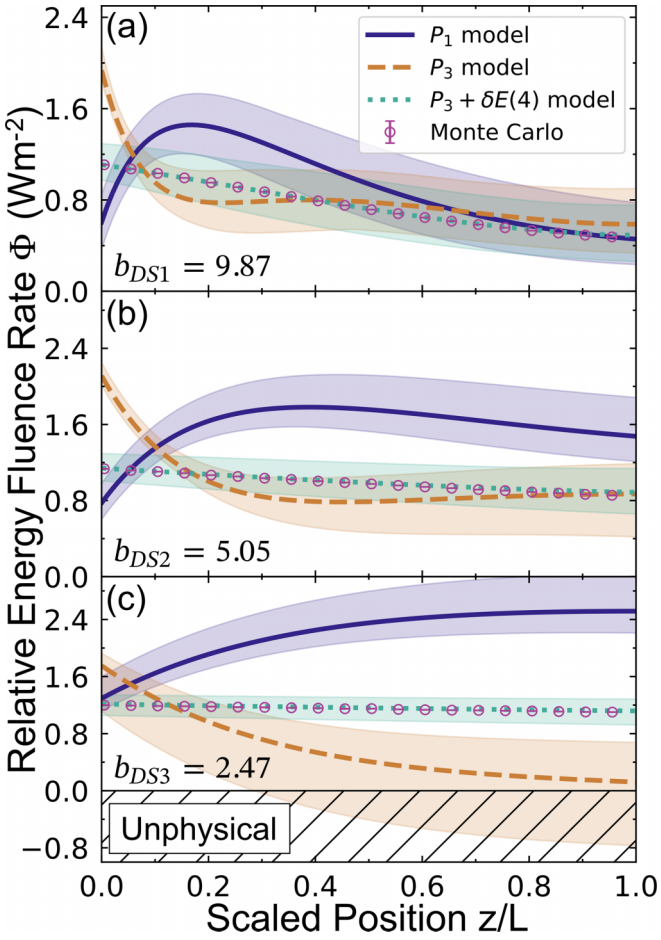

FIG. 10. Modeled position-dependent energy fluence rate $\Phi(z)$ for samples (a) DS1, (b) DS2, and (c) DS3. The horizontal axis represents the z positions scaled by the thickness of the sample. The vertical axis displays the modeled relative $\Phi(z)$. Lines represent the results of the P_N approximations and the circles represent the results of Monte Carlo simulations. In (c) the unphysical area where Φ is negative is marked by black hatched lines.

The results of the P_1, P_3, and $P_3 + \delta$E(4) approximations and Monte Carlo simulations are illustrated in Fig. 10, where the z positions are scaled by the thickness of the sample, and the modeled $\Phi(z)$ is relative, as the incident flux density (irradiance) in the models is set to be $F_0 = 1$. The dynamic ranges of the P_N approximations represent the modeled values for the extracted $(a,\ g)$ range. Initially, it may appear confusing that a relative result is greater than 1, as seen in the case of sample DS1. Although both the irradiance F_0 and energy fluence rate Φ have the same units W m^{-2}, the former denotes the optical power through the surface of a flat unit area in the direction normal to the surface, while the latter refers to the total optical power through a spherical unit surface area in all directions [72]. Therefore, depending on the scattering properties of the medium under study, it is possible for Φ to exceed the incident irradiance [17,73,74].

Figure 10 shows that the $P_3 + \delta E(4)$ approximation agrees best with the Monte Carlo simulations, consistent with previous reports [17,45]. The P_1 and P_3 approximations perform poorly for these anisotropically scattering and absorbing samples, and the P_3 approximation even predicts an unphysical negative-energy fluence rate for the dynamic range of the optically thin sample DS3. The unphysical results of the P_3 approximation for sample DS3 also agree with our previous findings [45], which shows a broader unphysical range of P_3 for optically thin samples in the strong-forward-scattering range, compared to the thicker samples.

D. Position-dependent energy fluence rate of undyed microsphere suspensions

We present measured $\Phi(z)$ of undyed sphere suspensions and compare them to models in Fig. 11. The P_N approximation results do not have dynamic ranges in Fig. 11 as the (a, g) pair of samples US1, US2, and US3 are extracted from exact Mie calculations, as explained in Sec. III B. Similar to Fig. 9, the horizontal axis denotes the z positions scaled by the thick-

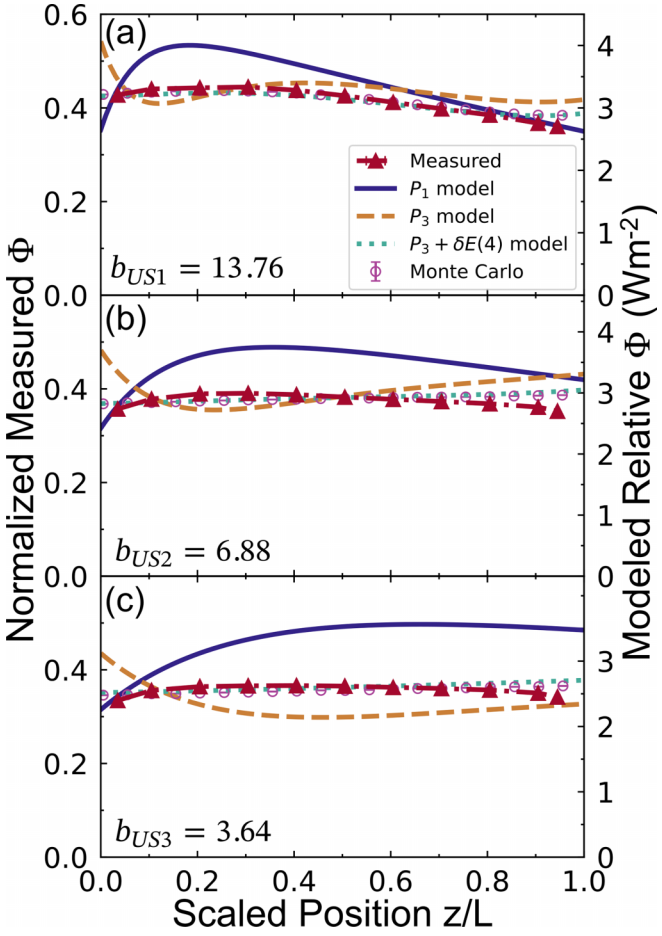

FIG. 11. Comparison of observations and models for samples (a) US1, (b) US2, and (c) US3. The abscissa represents the z position scaled by the sample thickness. The left ordinate displays the $\Phi(z)$ measurements of samples normalized to the measured incident intensity. The right ordinate corresponds to the modeled relative $\Phi(z)$. The red triangles connected by dash-dotted lines represent the measured results of samples. The measured results are calculated by integrating the y scans at each z position, shown as triangles. Curves are the results of the P_N approximations and purple circles are the results of Monte Carlo simulations.

ness of the sample and the left vertical axis gives the $\Phi(z)$ measurements of samples normalized to the measurements of the incident intensity given in Fig. 12(b). The right vertical axis is the modeled relative $\Phi(z)$, and both vertical axes are scaled to compare the trends of measured and modeled Φ. Good agreement between the trends of $P_3 + \delta E(4)$, Monte Carlo, and measurements is observed. For these microspheres no unphysical predictions occur since the absorption is absent; hence the albedo is equal to 1. Differences due to experimental limitations are discussed in Sec. III E.

E. Experimental limitations

Systematic errors are inevitable in any experiment, including the measurements of $\Phi(z)$. It is thus important to identify and comprehend the underlying causes of the systematic errors, before claiming that the measurements reflect reality. Hence, this section discusses the limitations of our experiment that affect the scaling value K for Eq. (5).

Our discussion starts with the shift in detected peaks for y scans at different z positions, which is not immediately obvious for scans presented in Fig. 18. To clarify this effect, y scans by the probe at specific z are presented in Fig. 12(a), which demonstrate a clear shift of the detected intensity in the y direction. This shift is caused by the probe moving at a small angle with respect to the z axis. The angle is estimated as approximately $\theta_z = 0.63^\circ$, considering the peaks movement of 0.1 mm in the y direction for a 9.1 mm travel in the z direction. Furthermore, Fig. 12(b) presents the incident intensity detected by the probe in air, which is used to normalize the measurements of samples in order to compensate for the effect of the y shift.

Other experimental limitations associated with the measurements with the probe are listed as follows.

(i) The capillary filled with quantum dots is not exactly parallel to the x axis given in Fig. 4. Although the kinematic mount attached to the probe holder, as shown in Fig. 5, is utilized to adjust the capillary angle, perfect alignment is not always achieved. As a result, the probe positioning inside the sample is restricted to a range between $z = 0.35$ and 9.75 mm for the z direction. In the event that the probe approaches the boundaries beyond these limits, the capillary may come into contact with the quartz walls of the cuvette, potentially causing its displacement or, worse, breaking of the capillary.

(ii) The stabilities of the probe holder, sample holder, and fiber-optic cable that connects the probe and detector are not perfect. Small variances in different scan directions presented in Fig. 16 are likely caused by this. However, even slight changes in the adjustment of these elements can lead to drastic changes in the detected intensity. Therefore, it is crucial to normalize the measurements to the incident intensity measured under identical conditions to the sample measurements. The measurements presented in this work are conducted with utmost care to address this issue.

(iii) The finite dimensions of the cuvette used in our experiments differ from ideal slab geometry, as a slab has an infinite xy plane. However, the beam diameter of our source ($d_{\text{beam}} \approx 1$ mm) is significantly smaller than the inner xy dimensions of the cuvette (42.5 × 30 mm), rendering this effect negligible.

(iv) Although the measurement of $\Phi(z)$ along the xy plane is carried out through y scans of the samples, the scans are limited to the range from $y = -6$ to 6 mm with the beam centered at $y = 0$. This range is selected due to low signal strength beyond this range and to shorten the complete measurement time. The range restriction leaves 18 mm of unmeasured space on the y axis. Additionally, during the sample scans, the capillary tip is situated at a distance of approximately $x \approx 11$ mm from the cuvette's bottom. Consequently, the probe scans a rectangular area of dimensions 34×12 mm^2 within the cuvette. Hence, the portion of the scanned area to the full xy plane within the sample is $A_{\text{scan}} = 32\%$. However, the measurement of $\Phi(z)$ cannot be directly scaled with A_{scan} because the experiments employ a collimated beam as the source and detect most of the light within the cuvette, as evident by the low signal strength beyond the scan range (see Fig. 18). However, it is worth noting that the signal outside

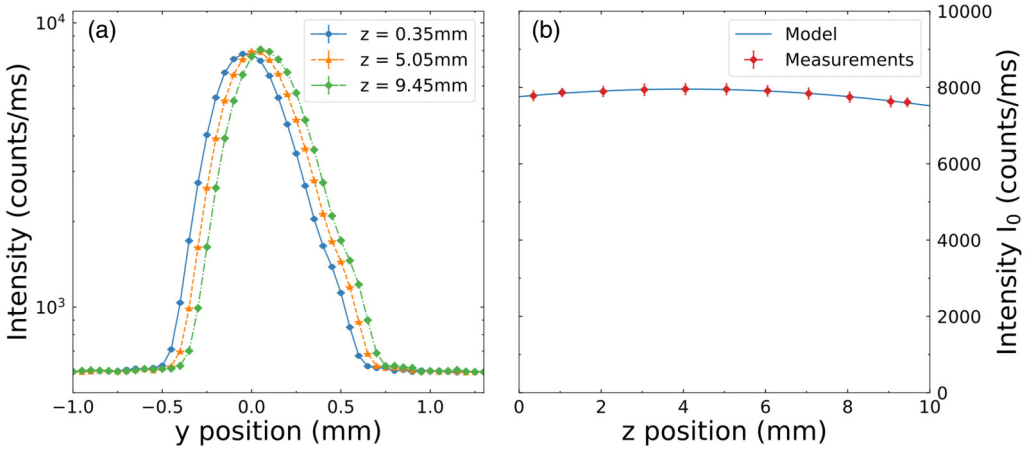

FIG. 12. (a) Probe scans in the y direction in the absence of a sample. This represents the incident beam profiles at the indicated z positions inside the sample. (b) Integrated y scans at specific z positions, in the absence of a sample. The blue line represents the polynomial fit to the measurements, to determine the incident beam intensity at all z positions.

the scanned range is higher for undyed samples, owing to the lower absorption by the scatterers compared to the dyed samples. Therefore, the scaling difference between the measured and modeled $\Phi(z)$ for undyed samples is greater than the one for dyed samples.

(v) The quantum dots inside the capillary have a certain quantum yield to convert absorbed blue light to emitted red light. This quantum yield is provided by the manufacturer as $\eta \geqslant 64\%$. Furthermore, the manufacturer specifies the molar extinction coefficient $\epsilon = 5.7 \times 10^6\ \mathrm{cm}^{-1}\,\mathrm{M}^{-1}$ and the molar concentration $c = 1.0 \pm 0.1\ \mu\mathrm{M}$. Using the inner diameter of the capillary that holds the quantum dots $d_{\mathrm{inner}} = 100\ \mu\mathrm{m}$ and the Beer-Lambert-Bouguer law, we calculate the extinction E_{qdots} to be

$$E_{\mathrm{qdots}} = \epsilon c d_{\mathrm{inner}} = 57 \tag{6}$$

and the optical thickness b_{qdots} to be

$$b_{\mathrm{qdots}} = E_{\mathrm{qdots}} \ln(10) = 131.2. \tag{7}$$

(vi) The presence of the probe inside the sample has an impact on light transport within the medium. In order to investigate this effect, the unscattered transmission T_{u} of the probe is measured[4] while scanning in the y direction at various z positions inside sample Ref (see Table I). The obtained results are illustrated in Fig. 13. Based on Fig. 13, the extinction coefficient of the probe is derived as $\mu_{\mathrm{ext}} = 4.8\ \mathrm{mm}^{-1}$ when the probe is situated at the center of the beam. The μ_{ext} represents the sum of absorption and scattering by the probe; hence the absorbed portion of light by the probe and quantum dots inside cannot be estimated by this measurement alone.

(vii) Part of the emitted light propagates through the capillary and emerges from its top, where it is coupled to the fiber-optic cable of the spectrometer via a connector manufactured in the workshop of the University of Twente. This connector, visible in Fig. 5, introduces a distance of approximately $d_{\mathrm{cap\text{-}fiber}} \approx 5$ mm between the capillary and the fiber. Assuming that the light emanates from the capillary with a solid angle of 2π and taking into account the core diameter of the fiber-optic cable (600 μm), straightforward calculations yield a coupling efficiency of $\eta_{\mathrm{coup}} = 2\%$ between the capillary and the fiber.

All experimental limitations listed above contribute to the deviation of measurement results to the model predictions in scale, and the parameter K in Eq. (5) is introduced to capture these effects.

IV. CONCLUSION

In this work, we have presented a comprehensive analysis of the experimental measurements of the position-dependent energy fluence rate in three-dimensional scattering samples with anisotropically scattering and absorbing microspheres ($r = 0.5$ μm), with and without absorbing dye. A thin capillary filled with quantum dots was used as a probe to measure the position-dependent energy fluence rate inside the samples, and the results were compared to analytical models and Monte Carlo simulations. The analytical P_1 and P_3 approximations to

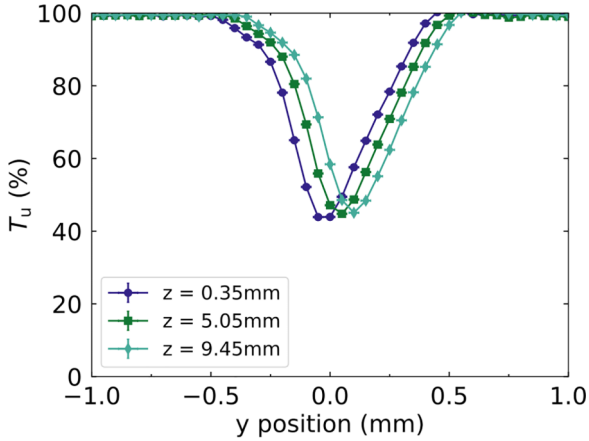

FIG. 13. Unscattered transmission T_{u} of the probe scanning the y direction at various z positions inside sample Ref (see Table I).

[4]This measurement is conducted with a capillary similar to the one used in the measurements of $\Phi(z)$.

the radiative transfer equation predicted inaccurate (and even unphysical) results for these samples, which have a range of scatterer densities. The albedo and anisotropy parameters for the dyed samples were extracted from both experiments and Monte Carlo simulations, while Mie calculations were used to determine the parameters for the undyed samples.

Notably, the P_1 and P_3 approximations failed to match the trends observed in the position-dependent fluence rate, as anticipated. In contrast, the Monte Carlo simulations and the $P_3 + \delta E(4)$ approximation, which did not yield unphysical results for the samples under consideration, exhibited relatively good agreement with the measured trends of the fluence rate. We provided a detailed discussion of the experimental limitations that prevent an absolute measurement, and an exact match with the models.

The data used for this publication are available via the open-access repository Zenodo database that is developed under the European OpenAIRE program and operated by CERN [75].

ACKNOWLEDGMENTS

We thank C. Harteveld and M. Goodwin for their help in sample preparation and building the experimental setup, M. Vretenar for three-dimensionally printing parts for the experimental setup, and A. Kienle, S. Salama, J. de Boer, and G. Vissenberg for very helpful discussions. We thank the staff of the Design Lab and of the Rapid Prototyping Lab at the University of Twente for three-dimensionally printing sample holders for our experimental setup. This work was supported by the NWO-TTW Program No. P15-36, Free-form scattering optics, in collaboration with TUE and TUD and with industrial partners ASML, Demcon, Lumileds, Schott, Signify, and TNO, and by the MESA+ Institute's section Applied Nanophotonics (ANP).

APPENDIX A: INFRASTRUCTURE

1. Choice of light source

Extinction spectra of the diluted dyed microsphere suspension with a scatterer number density of $\rho = (4.6 \pm 0.6) \times 10^4$ mm^{-3} were measured using a UV-Vis spectrometer [Perkin Elmer Lambda 850 from the Molecular Nanofabrication (MNF) chair in Twente]. The measured spectrum is presented in Fig. 14. The sphere suspension is diluted with DI water; thus, the reference used in this UV-Vis measurement is also DI water. The extinction peak of the microspheres in the visible range is observed to be around 400 nm wavelength. Therefore, we chose a Thorlabs NPL41B nanosecond laser with a peak wavelength of $\lambda = 408.5$ nm as the light source in our experiments to minimize the albedo of the scatterers.

2. Preparation of the probe

An example of a probe filled with fluorescent reporters is depicted in Fig. 2. To realize such a probe, a cylindrical quartz capillary with 10 cm length (CM Scientific, CV1017Q-100), an outer diameter of 170 μm, and an inner diameter of 100 μm is utilized. Such a capillary is filled with quantum

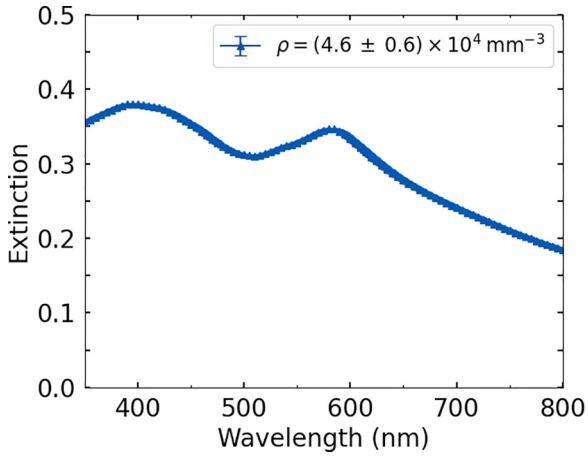

FIG. 14. Measured extinction of the dyed microsphere suspension with number density $\rho = (4.6 \pm 0.6) \times 10^4$ mm^{-3}.

dots suspended in decane (Thermo Fisher Qdot™ 655 ITK™ organic quantum dots). The quantum dots scatter and absorb the incident UV light and reemit in the red part of the visible spectrum, with a peak at $\lambda_{\text{peak}} = 665$ nm wavelength [see Fig. 15(b)]. To place the quantum dots inside the capillary, the capillary is placed in a teflon-lined fiber chuck (Newport FPH-J). A rubber stop is attached to the back end of the fiber chuck, and the quantum dots are sucked in the capillary using this assembly [see Fig. 15(a)]. Finally, both ends of the capillary are sealed with super glue, as shown in Fig. 15(c). In our study, the capillary-fiber chuck assembly is referred to as the probe.

3. Experimental procedures with the probe

Measurements with the probe along the z direction inside the sample DS1 are shown in Fig. 16, including the results from four primary scan directions: forward, forward side, random, and random side. To prevent collisions with the sample holder that would damage the fragile probe, the scans start at $z = 0.05$ mm and end at $z = 9.75$ mm. The forward direction indicates that the sample is scanned from the left boundary ($z = 0$) to the right boundary ($z = 10$), while forward side refers to scanning the sample in the same direction as forward in z, as well as scanning it in the y direction at specific z

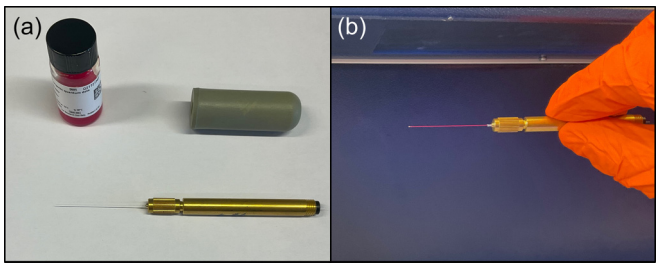

FIG. 15. Photograph of the preparation phases of the probe. (a) The quantum dots, the capillary held by the fiber chuck, and the rubber stop used for sucking quantum dots inside the capillary. (b) Red emission is observed when the capillary is illuminated with UV light.

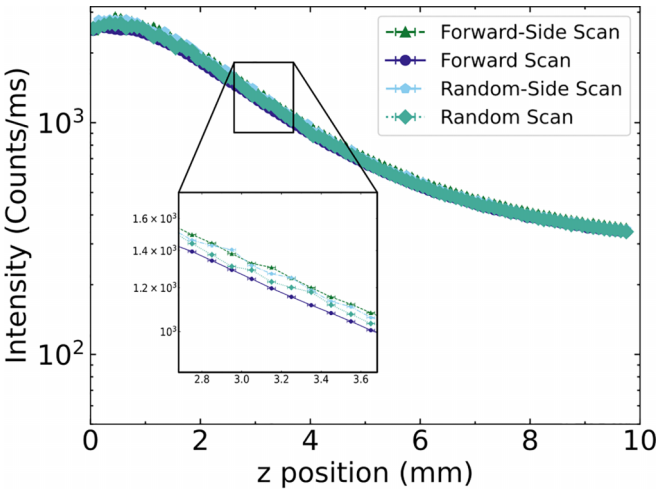

FIG. 16. Representative scans of the position-dependent intensity in the z direction in sample DS1, for four different scan directions. The vertical axis displays the measured intensity and the horizontal axis shows the position in the z direction. The inset highlights the small differences between scans.

positions. Random direction refers to scans of the sample along the z direction with the probe randomly positioned during the scan. Finally, random side indicates that the sample is scanned in the same way as in random direction, but in addition it is scanned in the y direction at specific z positions and the y scans are also done with a random positioning of the probe. Figure 16 shows that the scan direction has minimal influence on the outcomes. The minor differences are attributed to slight instabilities of the probe holder, which are discussed further in Sec. III E. Figure 17 presents the position-dependent intensity in the z direction for samples DS1, DS2, and DS3. The data points in Fig. 17 represent an average of four different scan directions, as elaborated in Fig. 16. Notably, the optically thicker samples exhibit a higher intensity than the thinner samples, up to a depth of approximately 2 mm inside

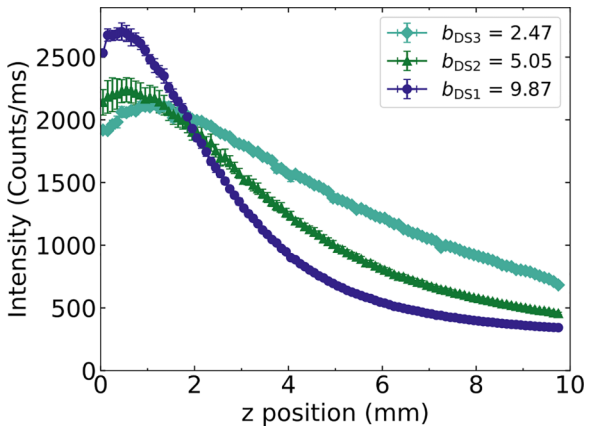

FIG. 17. Position-dependent intensity in the z direction detected inside dyed microsphere suspensions DS1, DS2, and DS3. The vertical axis displays the measured intensity and the horizontal axis shows the position in the z direction. The optical thicknesses of the samples are given in the legend. Data points represent the averages of four scans in different directions (see Fig. 16).

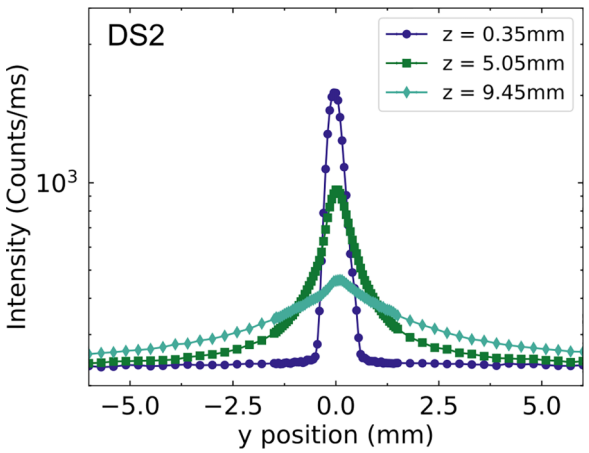

FIG. 18. Representative scans of the y direction at specific z positions inside sample DS2. The vertical axis displays the measured intensity and the horizontal axis shows the position in the z direction.

the sample. This behavior is attributed to the increased number of scatterers in the thicker samples, which scatter the light into the probe more than the less dense samples at the first few millimeters. After $z = 2$ mm depth, the trend reverses and the densest sample has the lowest detected intensity. This trend is expected, as the extinction is higher for thicker samples. However, it should be noted that while the probe scans the z direction entirely in this measurement, it is insufficient to fully characterize the $\Phi(z)$, since a large portion of the xy plane is not measured. The models simplify the problem to one dimension by utilizing the symmetries within the slab and averaging over the xy plane at each z position [45]. The diameter of our probe is 170 μm, while the beam size is approximately 1 mm, and the z scans are done when the probe is at the center of the beam in the y direction. Consequently, although the probe's length in the x direction is roughly 40 mm within the sample, the scan presented in Fig. 17 predominantly collects the unscattered intensity.

In order to obtain a more comprehensive understanding of $\Phi(z)$, it is necessary to scan samples in the y direction at various positions in z. Figure 18 presents three scans at specific z positions. The results show that the energy distribution broadens in the y direction as the light travels deeper in z, in agreement with expectations from multiple scattering [67,76–78]. All samples are probed in the y direction at numerous z positions, and the resulting curves obtained from these y scans at each z position are integrated to derive a value that represents the total $\Phi(z)$ integrated over an xy plane. Figure 19 shows the integrated y scans of sample DS2, where the z positions are scaled by the thickness of the sample and the measured $\Phi(z)$ is normalized by the incident intensity. Notably, Fig. 19 illustrates the inclusion of diffuse light to the detection, in contrast to the measurements obtained solely from z scans, as shown in Fig. 17.

APPENDIX B: THEORY BACKGROUND

Transport theory describes the propagation of light in complex media using the well-known radiative transfer equation (RTE) [23–26,79–81]. Whereas in transport theory

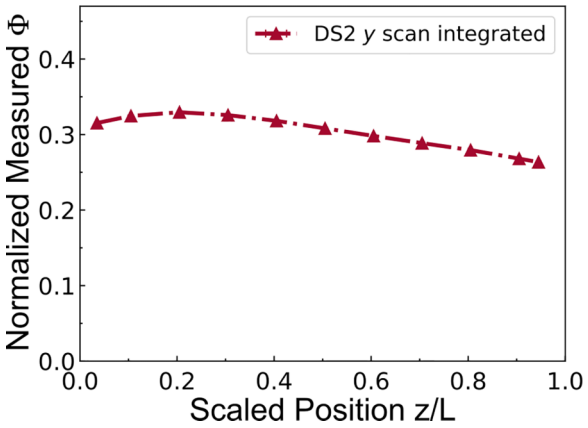

FIG. 19. Representative integrated y scans at specific z positions inside sample DS2. The vertical axis displays the $\Phi(z)$ measurements of samples normalized to the measurements of the incident intensity. The horizontal axis represents the z positions scaled by the thickness of the sample.

one neglects the wave nature and concomitant interference of light (speckle), the RTE is widely used as it generally provides a robust description [66,78]. The most fundamental quantity described by the RTE is the specific intensity $I(\mathbf{r}, \hat{\mathbf{s}})$ that describes the average power flux density at position $\mathbf{r}$ in a given direction $\hat{\mathbf{s}}$, within a unit solid angle and a unit frequency band. It is challenging to solve $I(\mathbf{r}, \hat{\mathbf{s}})$ directly, as it depends on both the position $\mathbf{r}$ and the direction $\hat{\mathbf{s}}$. Therefore, analytical approximations to the RTE or Monte Carlo simulations are preferred.

1. P_N approximations

The so-called P_N approximation is a widely used analytical approximation to the RTE, where the dependence on both variables $(\mathbf{r}, \hat{\mathbf{s}})$ is separated [80] by expanding $I(\mathbf{r}, \hat{\mathbf{s}})$ in products of complete sets on the domains of $\mathbf{r}$ and $\hat{\mathbf{s}}$,

$$I(\mathbf{r}, \hat{\mathbf{s}}) = \sum_{l=0}^{N} \sum_{m=-l}^{l} \psi_l^m(\mathbf{r}) Y_l^m(\hat{\mathbf{s}}). \tag{B1}$$

Here $\psi_l^m(\mathbf{r})$ are the spatial components, $Y_l^m(\hat{\mathbf{s}})$ are the directional components taken as the Laplace spherical harmonics [82,83], and N is the order of the approximation that determines the number of terms in Eq. (B1). In particular, the P_1 approximation is well known as it corresponds to the widely used diffusion approximation [66,78]. The analytical P_N approximations are mostly used for simple sample geometries such as a slab and a sphere and their accuracies depend notably on (i) the order N of the approximation, (ii) the optical properties of the medium, and (iii) the scattering phase function used in the approximation.

2. Boundary conditions

In this work, we apply Marshak-type boundary conditions [84] to solve the RTE for a slab geometry. The boundary conditions assume that on the boundaries, no diffuse light enters the scattering medium from the surrounding medium outside. When the refractive indices of the media inside and outside do not match, the total diffuse flux at the boundary directed into the medium is the part of the outwardly directed flux that is reflected by the surface [17,38,39,43,85]. This conservation law results in two boundary conditions

$$\int_0^1 I_{\text{diff}}(0, \mu) P_l(\mu) d\mu = \int_0^1 R(\mu) I_{\text{diff}}(0, -\mu) P_l(\mu) d\mu, \tag{B2}$$

$$\int_{-1}^0 I_{\text{diff}}(L, -\mu) R(-\mu) P_l(\mu) d\mu = \int_{-1}^0 I_{\text{diff}}(L, \mu) P_l(\mu) d\mu, \tag{B3}$$

where L is the sample thickness, $R(\mu)$ the specular Fresnel reflection function for unpolarized light, I_{diff} the diffuse specific intensity, and μ the directional cosine of light. In addition, P_l is a Legendre polynomial and l specifies the order of the approximation.

In our experiments, the microsphere suspensions are held inside quartz cuvettes during measurements. We modify the boundary conditions in Eqs. (B2) and (B3) by introducing a reflection coefficient that accounts for the internal reflections from the quartz walls surrounding the samples. The reader is referred to Ref. [62] for details about this modification and the full derivation of the P_N approximations used in this work.

[1] E. F. Schubert, *Light-Emitting Diodes*, 2nd ed. (Cambridge University Press, Cambridge, 2006).

[2] M. R. Krames, O. B. Shchekin, R. Mueller-Mach, G. O. Mueller, L. Zhou, G. Harbers, and M. G. Craford, J. Display Technol. **3**, 160 (2007).

[3] H. Bechtel, P. Schmidt, W. Busselt, and B. S. Schreinemacher, in *Proceedings of the Eighth International Conference on Solid State Lighting, San Diego, 2008*, edited by I. T. Ferguson, T. Taguchi, I. E. Ashdown, and S.-J. Park (SPIE, Bellingham, 2008), Vol. 7058, pp. 64–73.

[4] I. Akasaki, Rev. Mod. Phys. **87**, 1119 (2015).

[5] H. Amano, Rev. Mod. Phys. **87**, 1133 (2015).

[6] S. Nakamura, Rev. Mod. Phys. **87**, 1139 (2015).

[7] M. L. Meretska, G. Vissenberg, A. Lagendijk, W. L. IJzerman, and W. L. Vos, ACS Photonics **6**, 3070 (2019).

[8] C.-C. Lin, Y.-R. Wu, H.-C. Kuo, M. Wong, S. Denbaars, S. Nakamura, A. Pandey, Z. Mi, P. Tian, K. Ohkawa, D. Iida, T. Wang, Y. Cai, J. Bai, Z. Yang, Y. Qian, S.-T. Wu, J. Han, C. Chen, and Y.-H. Fang, J. Phys.: Photonics **5**, 042502 (2023).

[9] T. Nousiainen and K. Kandler, in *Light Scattering Reviews 9: Light Scattering and Radiative Transfer*, edited by A. Kokhanovsky, Springer Praxis Books (Springer, Berlin, 2015), pp. 3–52.

[10] C. J. Funk, Appl. Opt. **12**, 301 (1973).

[11] W. L. Vos, M. Donze, and H. Buiteveld, Commun. Sanitary Eng. Water Manag. **7**, 86 (1986).

[12] G. R. Fournier and J. L. Forand, P. Soc. Photo. Opt. Ins. **2258**, 194 (1994).

[13] F. Fell and J. Fischer, J. Quant. Spectrosc. Radiat. Transfer **69**, 351 (2001).

[14] D. Stramski, E. Boss, D. Bogucki, and K. J. Voss, Prog. Oceanogr. **61**, 27 (2004).
[15] N. J. McCormick, in *Computational Methods in Transport*, edited by F. Graziani (Springer, Berlin, 2006), pp. 151–163.
[16] M. S. Salama and W. Verhoef, Remote Sens. Environ. **157**, 111 (2015).
[17] W. M. Star, in *Dosimetry of Laser Radiation in Medicine and Biology*, edited by G. J. Mueller, D. H. Sliney, and R. F. Potter (SPIE, Bellingham, 1989), Vol. 10305, pp. 147–155.
[18] B. C. Wilson and S. L. Jacques, IEEE J. Quantum Electron. **26**, 2186 (1990).
[19] W. F. Cheong, S. A. Prahl, and A. J. Welch, IEEE J. Quantum Electron. **26**, 2166 (1990).
[20] A. Kienle and R. Hibst, Phys. Rev. Lett. **97**, 018104 (2006).
[21] J. C. J. Paasschens, M. J. M. de Jong, P. W. Brouwer, and C. W. J. Beenakker, Phys. Rev. A **56**, 4216 (1997).
[22] R. Pierrat and R. Carminati, Phys. Rev. A **76**, 023821 (2007).
[23] P. Wang, S. R. Arridge, and M. Jiang, Phys. Rev. A **90**, 023803 (2014).
[24] K. Vynck, R. Pierrat, and R. Carminati, Phys. Rev. A **94**, 033851 (2016).
[25] F. Tommasi, L. Fini, F. Martelli, and S. Cavalieri, Phys. Rev. A **102**, 043501 (2020).
[26] T. J. Arruda, A. S. Martinez, and F. A. Pinheiro, Phys. Rev. A **98**, 043855 (2018).
[27] S. A. Prahl, M. Keijzer, S. L. Jacques, and A. J. Welch, in *Dosimetry of Laser Radiation in Medicine and Biology*, edited by G. J. Mueller, D. H. Sliney, and R. F. Potter, International Society for Optics and Photonics (SPIE, Bellingham, 1989), Vol. 10305, pp. 105–114.
[28] S. Mujumdar, R. Torre, H. Ramachandran, and D. S. Wiersma, J. Nanophotonics **4**, 041550 (2010).
[29] S. L. Jacques, in *Optical-Thermal Response of Laser-Irradiated Tissue*, edited by A. J. Welch and M. J. C. van Gemert (Springer, Dordrecht, 2011), pp. 109–144.
[30] M. Atif, A. Khan, and M. Ikram, Opt. Spectrosc. **111**, 107 (2011).
[31] R. Uppu and S. Mujumdar, Phys. Rev. A **87**, 013822 (2013).
[32] A. A. Leino, A. Pulkkinen, and T. Tarvainen, OSA Continuum **2**, 957 (2019).
[33] J. Jönsson and E. Berrocal, Opt. Express **28**, 37612 (2020).
[34] M. G. Cooper, L. C. Smith, A. K. Rennermalm, M. Tedesco, R. Muthyala, S. Z. Leidman, S. E. Moustafa, and J. V. Fayne, Cryosphere **15**, 1931 (2021).
[35] A. Krieger and S. Wolf, Astron. Astrophys. **645**, A143 (2021).
[36] R. W. Shonkwiler and F. Mendivil, *Explorations in Monte Carlo Methods* (Springer, New York, 2009).
[37] J. H. Joseph, W. L. Wiscombe, and J. A. Weinman, J. Atmos. Sci. **33**, 2452 (1976).
[38] W. M. Star, J. P. A. Marijnissen, and M. J. C. van Gemert, Phys. Med. Biol. **33**, 437 (1988).
[39] M. Keijzer, W. M. Star, and P. R. M. Storchi, Appl. Opt. **27**, 1820 (1988).
[40] D. Dickey, O. Barajas, K. Brown, J. Tulip, and R. B. Moore, Phys. Med. Biol. **43**, 3559 (1998).
[41] H. Egger and M. Schlottbom, Appl. Anal. **93**, 1283 (2014).
[42] A. Liemert and A. Kienle, Phys. Rev. A **83**, 015804 (2011).
[43] A. Liemert, S. Geiger, and A. Kienle, J. Opt. Soc. Am. A **38**, 405 (2021).
[44] F. Ott, D. Reitzle, B. Krüger, A. Liemert, and A. Kienle, J. Quant. Spectrosc. Radiat. Transfer **277**, 107987 (2022).
[45] O. Akdemir, A. Lagendijk, and W. L. Vos, Phys. Rev. A **105**, 033517 (2022).
[46] G. Dolgos and J. V. Martins, Opt. Express **22**, 21972 (2014).
[47] R. Boiger, R. L. Modini, A. Moallemi, D. Degen, A. Adelmann, and M. Gysel-Beer, J. Aerosol Sci. **163**, 105977 (2022).
[48] Q. Chen, Q. Chen, S. Liu, and X. Luo, IEEE Trans. Device Mater. Reliab. **14**, 645 (2014).
[49] W. M. Star, H. P. A. Marijnissen, H. Jansen, M. Keijzer, and M. J. C. van Gemert, Photochem. Photobiol. **46**, 619 (1987).
[50] N. Pomerleau-Dalcourt and L. Lilge, Phys. Med. Biol. **51**, 1929 (2006).
[51] T. C. Zhu, M. M. Kim, J. Padawer, A. Dimofte, M. Potasek, K. Beeson, and E. Parilov, in *Optical Methods for Tumor Treatment and Detection: Mechanisms and Techniques in Photodynamic Therapy XXVII*, edited by D. H. Kessel and T. Hasan, SPIE Proc. (SPIE, Bellingham, 2018), Vol. 10476.
[52] Freeform scattering optics, initiative by 3 Dutch universities, https://www.freeformscatteringoptics.com/ (2016).
[53] R. Horstmeyer, H. Ruan, and C. Yang, Nat. Photonics **9**, 563 (2015).
[54] P. Hong, O. S. Ojambati, A. Lagendijk, A. P. Mosk, and W. L. Vos, Optica **5**, 844 (2018).
[55] A. Daniel, D. Oron, and Y. Silberberg, Opt. Express **27**, 21778 (2019).
[56] M. Megens, C. M. van Kats, P. Bösecke, and W. Vos, Langmuir **13**, 6120 (1997).
[57] D. O. Riese, G. H. Wegdam, W. L. Vos, R. Sprik, D. Fenistein, J. H. H. Bongaerts, and G. Grübel, Phys. Rev. Lett. **85**, 5460 (2000).
[58] M. Megens and W. L. Vos, Phys. Rev. Lett. **86**, 4855 (2001).
[59] A. Hartsuiker and W. L. Vos, Langmuir **24**, 4670 (2008).
[60] W. L. Vos, Ph.D. thesis, University of Amsterdam, 1991.
[61] L. F. Rojas-Ochoa, J. M. Mendez-Alcaraz, J. J. Sáenz, P. Schurtenberger, and F. Scheffold, Phys. Rev. Lett. **93**, 073903 (2004).
[62] O. Akdemir, Ph.D. thesis, University of Twente, 2023.
[63] X. Li, J. M. Zhao, C. C. Wang, and L. H. Liu, Appl. Opt. **55**, 8171 (2016).
[64] J. Olmos-Trigo, C. Sanz-Fernández, D. R. Abujetas, J. Lasa-Alonso, N. de Sousa, A. Garcia-Etxarri, J. A. Sánchez-Gil, G. Molina-Terriza, and J. J. Sáenz, Phys. Rev. Lett. **125**, 073205 (2020).
[65] K. L. van der Molen, P. Zijlstra, A. Lagendijk, and A. P. Mosk, Opt. Lett. **31**, 1432 (2006).
[66] M. C. W. van Rossum and T. M. Nieuwenhuizen, Rev. Mod. Phys. **71**, 313 (1999).
[67] E. Akkermans and G. Montambaux, *Mesoscopic Physics of Electrons and Photons* (Cambridge University Press, Cambridge, 2007).
[68] W. L. Vos, T. W. Tukker, A. P. Mosk, A. Lagendijk, and W. L. IJzerman, Appl. Opt. **52**, 2602 (2013).
[69] A. Rates, Ph.D. thesis, University of Twente, 2023.
[70] X. Ma, J. Q. Lu, R. S. Brock, K. M. Jacobs, P. Yang, and X.-H. Hu, Phys. Med. Biol. **48**, 4165 (2003).
[71] L. G. Henyey and J. L. Greenstein, Astrophys. J. **93**, 70 (1941).
[72] E. Henderson, B. Lai, and L. Lilge, in *Data Acquisition*, edited by M. Vadursi (IntechOpen, Rijeka, 2010), Chap. 14.
[73] S. L. Jacques, Photochem. Photobiol. **67**, 23 (1998).

[74] Y. H. Ong and T. C. Zhu, Opt. Express **24**, 26261 (2016).
[75] https://zenodo.org/records/10534239.
[76] A. F. Koenderink and W. L. Vos, J. Opt. Soc. Am. B **22**, 1075 (2005).
[77] B. P. J. Bret, Ph.D. thesis, University of Twente, 2005.
[78] R. Carminati and J. C. Schotland, *Principles of Scattering and Transport of Light* (Cambridge University Press, Cambridge, 2021).
[79] S. Chandrasekhar, *Radiative Transfer* (Dover, New York, 1960).
[80] J. H. Tait, *An Introduction to Neutron Transport Theory* (Longmans, London, 1964).
[81] A. Ishimaru, *Wave Propagation and Scattering in Random Media* (Academic, New York, 1978), Vols. I and II.
[82] J. D. Jackson, *Classical Electrodynamics* (Wiley, New York, 1998).
[83] G. B. Arfken and H. J. Weber, *Mathematical Methods for Physicists* (Elsevier, Boston, 2005).
[84] M. F. Modest, *Radiative Heat Transfer* (Academic, London, 2003).
[85] A. Liemert and A. Kienle, Med. Phys. **41**, 111916 (2014).